J Nanopart Res (2017) 19:231
DOI 10.1007/s11051-017-3931-6

RESEARCH PAPER

Surfactant-assisted production of $TbCu_2$ nanoparticles

M. de la Fuente Rodríguez · J. I. Espeso · J. A. González · J. Rodríguez Fernández · D. P. Rojas · L. Rodríguez Fernández · A. Garcia-Arribas · M. L. Fdez-Gubieda · C. Echevarria-Bonet · É. A. Périgo · A. Michels · L. Fernández Barquín

Received: 12 January 2017 / Accepted: 15 June 2017

Abstract The production of surfactant-assisted metallic nanoparticles of $TbCu_2$ has been achieved by the combination of high-energy ball milling in tungsten carbide containers and the use of oleic acid ($C_{18}H_{34}O_2$) and heptane (C_7H_{16}). The alloys were first produced in bulk pellets by arc melting and subsequently milled for only 2 and 5 h in oleic acid (15 and 30% mass weight). The powders consist of an ensemble of nanoparticles with a $TbCu_2$ lattice cell volume of ≈215 Å^3, an average particle diameter between 9 and 12 nm and inhomogeneous lattice strain of 0.2–0.4%, as deduced from X-ray diffraction data. The nanometric sizes of the crystals with defined lattice planes are close to those obtained by transmission electron microscopy. Raman spectroscopy shows the existence of inelastic peaks between 1000 and 1650 cm^{-1}, a characteristic of $C_{18}H_{34}O_2$. The magnetisation shows a peak at the antiferromagnetic-paramagnetic transition with Néel temperatures around 48 K (below that of bulk alloy) and a distinctive metamagnetic transition at 5 K up to 40 K. The Curie-Weiss behaviour above the transition reveals effective Bohr magneton numbers (≈9.1–9.9 μ_B) which are close to what is expected for the free Tb^{3+} ion using Hund's rules. The metamagnetic transition is slightly augmented with respect to the bulk value, reaching H = 24.5 kOe by the combined effect of the size reduction and the lattice strain increase and the increase of magnetic disorder. At low temperatures, there is irreversibility as a result of the existing magnetic disorder. The moment relaxation follows an Arrhenius model with uncompensated Tb moments, with activation energies between 295 and 326 K and pre-exponential factors between 10^{-11} and 10^{-13} s. The results are interpreted as a consequence of the existence of a diamagnetic surfactant which drastically decreases the magnetic coupling between interparticle moments.

M. de la Fuente Rodríguez (✉) · J. I. Espeso · J. A. González · J. Rodríguez Fernández · L. Fernández Barquín
Dpto. CITIMAC, Universidad de Cantabria, 39005 Santander, Spain
e-mail: delafuente.rodriguez.maria@gmail.com

D. P. Rojas
Dpto. Estructuras y Física de Edificación. ETSAM, Universidad Politécnica de Madrid, 28040 Madrid, Spain

L. Rodríguez Fernández
SERMET, Universidad de Cantabria, 39005 Santander, Spain

A. Garcia-Arribas · M. L. Fdez-Gubieda
Dpto. Electricidad y Electrónica, Universidad País Vasco/EHU, 48080 Bilbao, Spain

C. Echevarria-Bonet
BCMaterials, Bizkaia Science and Technology Park, 48160 Derio, Spain

É. A. Périgo
ABB Corporate Research Center, 940 Main Campus Drive, Raleigh, NC 27606, USA

A. Michels
Physics and Materials Science Research Unit, University of Luxembourg, 1511 Luxembourg, Grand Duchy of Luxembourg

Published online: 28 June 2017

Keywords Rare Earth binary nanoparticles · Surfactant-assisted production · Superantiferromagnetism · Arrhenius relaxation · Synthesis

Introduction

Overwhelming research efforts have been focused on the development of nanostructures touching a varied technological transfer. This development has become possible due to the controlled tuning of physical properties through the modification of some key parameters, most notably the average nanostructure dimension (Moriarty 2001; Gleiter et al. 2014; Stark et al. 2015; Tartaj et al. 2003; Yadav et al. 2012; Mørup et al. 2011; Bedanta and Kleemann 2009). More and more frequently, the use of a combination of nanostructured materials may lead to both apparitions of new phenomena at the interfaces giving rise to multipurpose functionalities (Nogués et al. 2005; Cuellar et al. 2014). As a result, nanoscience has become a mature multidisciplinary research field in the last decade.

Nanostructured materials are produced in different forms and shapes as the modern production techniques allow for an increasing control at the nanoscale. Among all possibilities, nanoparticle systems stand out as they are relatively easy to produce and provide versatile applications. To achieve an effective application of nanoparticles, industrial re-scaling should be possible (Stark et al. 2015). Some production routes are more favourable, and among them, the chemical synthesis routes are widely spread despite the material yield is sometimes low (Tartaj et al. 2003). Other solid-state routes allow for the production of mass quantities of nanoparticles with a reasonable narrow size distribution of the particles. One of such is the high-energy ball milling technique in which commonly metallic nanoparticles are produced after some time of crushing of starting bulk materials. The latter technique is recognized within engineering processes, and thus, the technological transfer is assured. The milling technique has been successfully used to produce a variety of materials, but there has been an outstanding interest in the fabrication of magnetic nanoparticles (MNPs) (Yadav et al. 2012).

Investigation on MNPs started decades ago, but a strenuous effort is still maintained, as the basic understanding of the mechanisms controlling the potential applications are still object of debate (Mørup et al. 2011; Bedanta and Kleemann 2009). In most cases, the reduction of the particle size (diameter, D) increases the influence of the surface atoms and the atomic coordination is feeble compared to the core (or bulk). Under these circumstances, it is clear that magnetic disorder is promoted, and frequently, a core-shell structure appears. Just as it happens with thin films and layered systems, the core-shell interface plays a significant role, although its fine role is not so obvious as it is commonly conceived. This has become important only in recent years when the more delicate magnetic couplings have been revealed in the MNP systems (Nogués et al. 2005).

Recently, there are consistent investigations on MNPs of rare Earth (R)-based alloys (Zhou and Bakker 1995; Li et al. 2013; Morales et al. 2004; Wang et al. 2007; de Paula et al. 2016; Sánchez-Valdés et al. 2014; Rojas et al. 2007; Echevarria-Bonet et al. 2013; Echevarria-Bonet et al. 2015). These studies are much less widespread than the usual investigations of Fe, Ni, Co oxide MNPs (Tartaj et al. 2003; Estrader et al. 2013; Rinaldi-Montes et al. 2015), although some of these R-based alloys allow for technological transfer as permanent magnets or magnetocaloric materials (Wang et al. 2007; de Paula et al. 2016; Sánchez-Valdés et al. 2014). The basic attraction is conspicuous as R-based alloys are dependent on the magnetic exchange coupling between localized magnetic moments (related to the deeply buried *4f*-electrons) and display a rich variety of magnetic structures by changes of the R atoms and/or of the non-magnetic metal (Luong and Franse 1995). We have been lately investigating $TbCu_2$ alloys, which constitute a paradigmatic member of the extended RX_2 family (Echevarria-Bonet et al. 2013; Echevarria-Bonet et al. 2015). The $TbCu_2$ MNPs consist of an antiferromagnetic (AFM) core in which the magnetic moment is localized on the Tb^{3+} ions ($J = 6$) atoms. It is fair to remind here that AFM nanoparticles have been somewhat overlooked in comparison to those of ferro- or ferri-magnetic core, although they are extremely adequate to analyse the behaviour of surface spins (Mørup et al. 2011; Estrader et al. 2013; Rinaldi-Montes et al. 2015). Indeed, the combination of mismatched moments of AFM sublattices and surface moments give rise to magnetic disorder. Such disorder is observed in the thermal variation of magnetization to a low-temperature peak ($T_B \approx 11$ K) which is well below from that peak characteristic of

the Néel transition ($T_N \approx 50$ K). Overall, their behaviour can be understood as superantiferromagnetic (SAFM) MNPs (Echevarria-Bonet et al. 2013; Echevarria-Bonet et al. 2015). The concept behind is similar to the superspin glass and superferromagnetic behaviours found in other varied systems containing MNPs such as α-Fe_2O_3 (Hansen et al. 2000), Fe/γ-Fe_2O_3 (Chandra et al. 2012), δ-$(Fe_{0.67}Mn_{0.33})$OOH (Peddis et al. 2012), FeAg (Alba Venero et al. 2013) and γ-Fe_2O_3 (Andersson et al. 2015), to cite a few. The whole field was initiated by a detailed analysis of α-FeOOH (Mørup et al. 1983) and has been christened as supermagnetism. The topic is superbly reviewed in Bedanta and Kleemann (2009).

Consequently, the magnetic coupling between moments in the core of the particles and those on the particle spin surface is modified greatly by subtle modifications in the particle interfacial structure. The extended use of surfactant as a method to coat the MNPs is very common for applications in the biomedical field and the production of improved hard magnets (Lu et al. 2007; Berry and Curtis 2003). In this sense, several attempts have been performed to apply the surfactant-assisted ball milling method. This is a top down route to produce metallic systems with a number of surfactants including oleic acid, oleylamine and palmitic acid (Ullah et al. 2014). In this sense, and regarding research on *R* alloys, there are limited results with analysis which have been conducted in $Nd_2Fe_{14}B$ lately. Here, the *BH* energy product is modified when the particle size is around 10 nm (Simeonidis et al. 2011). Also, other common *R*-based permanent magnets, $SmCo_5$, (and closely related alloys) have also been studied, showing an increase of coercivity (H_c) reaching H_c = 18.6 kOe (Akdogan et al. 2009).

It is then straightforward to realize that there is a need to improve our understanding of the mechanisms acting in surfactant-coated *R*-based alloys. A reasonable choice is to use a common stoichiometry. Therefore, in this article, we are investigating the effect of production with surfactants on the MNPs focusing in particular on especially the modifications in the crystallographic structure, the MNPs size distribution and, concomitantly, the Néel temperature and the magnetic disorder. The results will be compared to the observations in *bare* superantiferromagnetic MNPs of $TbCu_2$ analysed comprehensively in Refs Echevarria-Bonet et al. (2013) and Echevarria-Bonet et al. (2015). In particular, the modifications will be understood to affect the magnetic relaxation of the $TbCu_2$ nanoparticles.

Production of surfactant-assisted $TbCu_2$ nanoparticles and structural and magnetic characterization methods

Magnetic nanoparticles of $TbCu_2$ were produced by means of the high-energy ball milling method adapted to the use of liquids. Basically, appropriate amounts of high-purity elements (Tb = 99.9% and Cu = 99.999%) were melted in an arc furnace, obtaining a pellet with a mass of about 5 g. The pellets were re-melted several times, sealed in quartz ampoule and then annealed in a furnace at 750 °C in vacuum ($\approx 10^{-2}$ mbar) for 5 days. Wide-angle X-ray diffraction (XRD) was employed in order to confirm the crystallographic structure of bulk $TbCu_2$ (orthorhombic $CeCu_2$-type, *Imma*). Finally, the pellet is crushed into powder and then inserted in o-ring sealed tungsten carbide (CW) containers.

The novelty aspect is related to the method used in order to obtain surfactant-assisted MNPs. Such a production route has previously been successfully employed to produce hard magnets of $SmCo_5$ and $Sm_2(Co_{0.8}Fe_{0.2})_{17}$ and has been adapted for our alloys (Akdogan et al. 2009). The milling process was carried out using a ball/sample weight ratio of 12:1, following successive clockwise and anti-clockwise rotation steps during 5 min with a spinning velocity of 200 rpm and 1 min of intermediate stops. Accurate amounts of oleic acid (99% purity, OA) as a surfactant and heptane (99.8%) as a milling medium were added in the CW containers. The amount of OA used was ≈15 and ≈30% of the weight of the starting metallic powder. Milled samples of $TbCu_2$ for 2 and 5 h were obtained for each of these proportions of oleic acid. Some of the samples were loaded in an Ar glove box and thus sealed. Hereafter, the representative samples will be labelled as OA15% 2 h and OA30% 2 h corresponding to the 2 h milled alloys and OA15% 5 h and OA30% 5 h to those milled for t = 5 h.

Structural analysis was procured by XRD which was performed in a Bruker D8 Advance diffractometer placing the micrometric milled powder on top of a Si-single [100] crystal sample holder. This type of holder is especially indicated in order to reduce the background signal. The XRD patterns were collected in the 18°–95° 2θ-angle range with 2θ-angle steps of 0.02° and an

integration time of 5 s/step. The XRD resolution function is crucial in order to extract reliable size and strain parameters (extracted diffraction peak broadening) in the Rietveld refinements (Rodríguez-Carvajal 1993). Such function has been calculated as the full width at half maximum (FWHM), according to $FWHM(2\theta) = \sqrt{U\tan^2\theta + V\tan\theta + W}$, with the aid of a LaB_6 calibration sample resulting in $U = 0.004098$, $V = -0.0026231$ and $W = 0.0030347$ as Caglioti's parameters. In consequence, the strain and size peak broadening is calculated, taking into account the instrumental broadening. To complete the structural analysis, transmission electron microscopy (TEM) was employed to estimate the nanoparticle crystallinity and the particle size distributions. A drop of the nanoparticle suspensions was deposited onto 300 mesh carbon copper grids and air-dried prior to observation. Images were acquired on a Jeol Jem 2100 equipped with an Oxford Inca X-stream EDX spectrometer operating at 200 kV. The particle size analysis was secured by IMAGE J software (Schneider et al. 2012). The OA presence was checked by Raman spectroscopy recorded with the T64000 micro-Raman spectrometer system (Horiba) together with the 514.5 nm green line of an Innova Spectrum 70 C Kripton-Argon laser (Coherent) and a nitrogen-cooled CCD (Jobin-Yvon Symphony) with a confocal microscope for the detection. The resolution was $\approx 1\ cm^{-1}$.

The magnetic properties have been revealed by the static and dynamic susceptibility measurements. The DC magnetization *M(T)* was recorded with a QD-PPMS magnetometer between 5 and 250 K in a standard zero field-cooled (ZFC) & field-cooled (FC) protocol with $H = 0.01$ T; isothermal magnetization *M(H)* curves were obtained at $T = 5$ and 40 K with fields reaching up to $H = 14$ T. The dynamic susceptibility (χ_{AC}) was recorded both in QD-MPMS and QD-PPMS instruments, recording data in a remarkably broad (five decades) range of frequencies f from $f = 0.1$ to $f = 10{,}000$ Hz. The amplitude of the oscillating AC field was set to $h = 3.13$ Oe.

Results and discussion

The initial pursuit is to disclose the structural state at the nanoscale. The crystallographic structure is ascertained by the XRD patterns. These are shown in Fig. 1 for the nano-$TbCu_2$ in both OA (15 and 30%) percentages and 2 and 5 h milling times. Rietveld refinements (FULLPROF program) of the XRD patterns allow establishing a precise structural sample knowledge, as crystallographic parameters are all evaluated simultaneously in patterns stemming from the whole (volume) sample. In this sense, the bulk crystallographic structure is retained (*Imma* space group) with Tb at 4e (0, 1/4, 0.538) and Cu at 8 h (0, 0.051, 0.165) ($CeCu_2$-type). The calculated function is a Thompson-Cox–Hastings pseudo-Voigt profile, well suited for size and strain calculations in MNPs (Schneider et al. 2012). The (standard) Bragg errors are very low ($R_B \leq 10\%$) for a MNP system, and consequently, the extracted values are of high quality. Our tests in XRD patterns for alloys milled under Ar atmosphere (not shown) show that the crystal structure is not modified with respect to those produced in air. The preparation in an inert gas environment using surfactants requires a careful container handling in a glove box. In view that no structural and magnetic modifications were observed in comparison to those produced in air, surely due to the protective coating by the surfactant, the results in the present work are concentrated on the latter samples.

The particle size (diameter, D) varies between $8\ nm < D < 12\ nm$, depending on the ($t = 2$ h, 5 h) milling time (see Table 1). Longer milling times result in smaller D, irrespective of the surfactant effect, and with further milling, it is expected that there would be an asymptotic value (Echevarria-Bonet et al. 2015). In the present case, the milling times are really short ($t \leq 5$ h), saving sample handling risk and costs. The XRD Rietveld refinement supports the presence of a group of $TbCu_2$ nanoparticles retaining the bulk orthorhombic structure within the cores, just as it did happen with the surfactant-free nano-$TbCu_2$ (Echevarria-Bonet et al. 2015). Notably, the comparison of the sizes achieved with the surfactant with those obtained in bare nanoparticles leads to the conclusion that more time is needed to reach the same particle size. For example, to obtain $D = 8$ nm, $t = 2$ h were employed for bare $TbCu_2$ nanoparticles (Echevarria-Bonet et al. 2015). It has been argued that the OA may reduce the re-welding and further increase of D of particles (Akdogan et al. 2009). Here, the reduction should be a consequence of the presence of oleic acid and heptane in the CW containers, decreasing the energy of the collisions between the ball and containers and the starting powders.

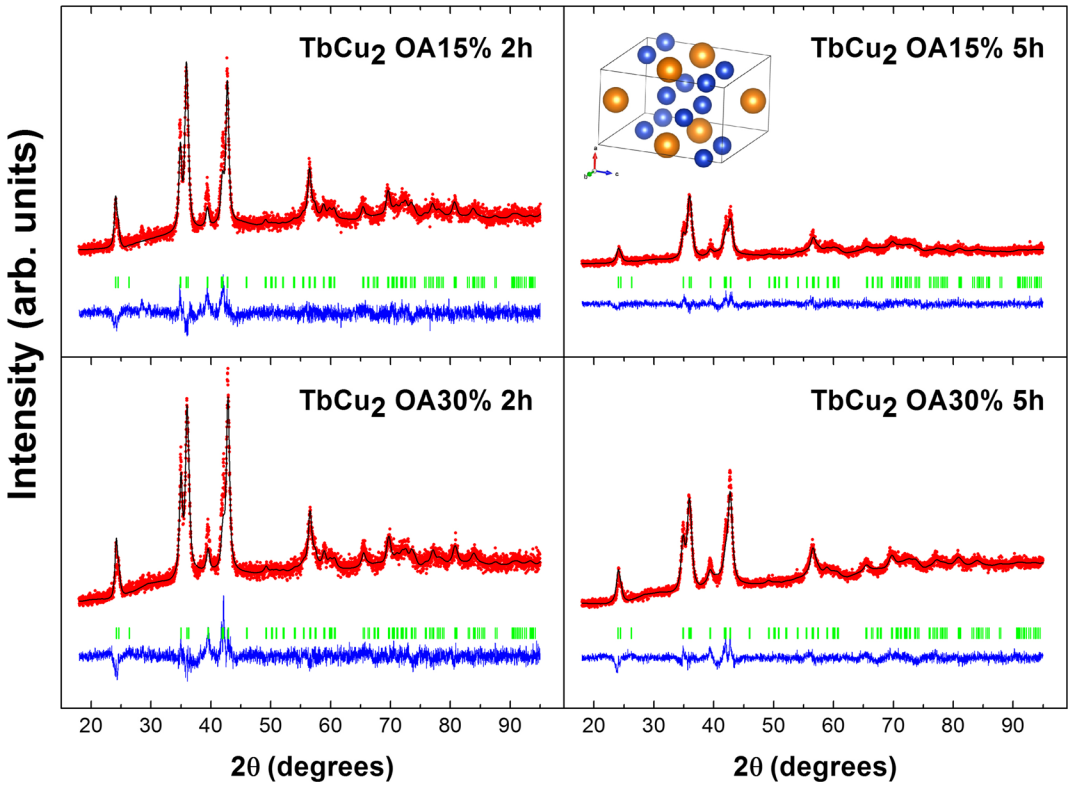

Fig. 1 X-ray diffraction patterns surfactant-assisted $TbCu_2$ nanoparticles milled for 2 and 5 h, with OA15% and OA30%. *Vertical lines* (*green*) indicate the Bragg reflections. The continuous (*black*) line is the Rietveld refinement using the bulk *Imma* crystallographic structure ($CeCu_2$-type). This structure is depicted (*top right*) with large Tb atoms (*gold*) and small Cu atoms (*blue*). The difference between the experimental and calculated patterns is depicted (*blue line*) below the vertical markers. The peak broadening is considerable and it is a consequence of the small nanoparticle size and the lattice strain

The volume of the cell remains practically unaltered at these short milling times (see Table 1); we observe only a marginal 1.4% reduction with respect to the bulk alloy ($V = 215.88$ Å^3). The tendency though is clear and points to a reduction of V (from $V \approx 215$ Å^3 to $V \approx 213$ Å^3) with the decrease of D in this surfactant-coated MNPs. As a reference, in bare $TbCu_2$ nanoparticles, $V = 215.62$ Å^3 for $D = 8$ nm (Echevarria-Bonet et al. 2015). It is common in milled MNPs to observe strain ($\eta \approx 0.3\%$) due to local lattice distortions; these are of the order of those alloys obtained without surfactant. The distortions are more likely to be present on the particle surface due to the lack of bond coordination (Echevarria-Bonet et al. 2015; Akdogan et al. 2009). A possible explanation of the decrease of lattice volume with milling might be connected with the existence of an "effective" pressure within the nanoparticles as a result of the lack of coordination of the surface atoms.

In any case, the interatomic distances between Tb^{3+} ions will remain practically the same to the bulk, and the magnetic coupling, thanks to the long-range indirect exchange interaction between localized *4f* Tb atoms, is not expected to vary from the bulk AFM coupling. The indirect exchange interaction, also known by Ruderman, Kittel, Kayusa, Yoshida (RKKY), provides the magnetic coupling among R ions. This coupling is due to the interaction between the localized spin of the 4f electrons with that of the conduction electron, and it was shown there exists an oscillating spin polarization, which extends to long distances and is affected by the Fermi vector. Effectively, this indirect coupling typically gives rise to ferromagnetic or antiferromagnetic coupling of the R ions precisely depending on the interatomic distance (Coey 2010).

The lack of variation of the AFM coupling between bulk and nanoparticle systems is confirmed by the values of the Néel temperature (see below), which are again very similar to the bulk value. To end with the structural analysis, the size distribution is provided by the TEM results. Representative images (see Fig. 2)

Table 1 Orthorhombic cell (*Imma*) parameters *a*, *b* and *c*; cell volume *V*, size *D* and strain η of $TbCu_2$ nanoparticles obtained by Rietveld refinement for surfactant-assisted $TbCu_2$ alloys at two milling times (*t*) and for two different amounts of Oleic Acid (% OA)

% OA	*t* (h)	*a* (Å)	*b* (Å)	*c* (Å)	*V* (Å^3)	*D* (nm)	R_B (%)	η (%)
15	2	4.3231(1)	6.8263(9)	7.3141(2)	215.8(4)	12(1)	9.5	0.2(1)
30	2	4.3168(7)	6.8252(4)	7.3099(8)	215.3(8)	11(1)	9.5	0.3(1)
15	5	4.2979(1)	6.7888(3)	7.2821(1)	212.4(7)	9(1)	6.5	0.4(1)
30	5	4.3038(3)	6.7939(5)	7.2899(2)	213.1(5)	9(1)	6.0	0.4(1)
Bulk		4.3165(1)	6.8223(3)	7.3202(3)	215.6(3)	–	23.1	–

The numbers in parenthesis indicate the uncertainty in the least significant figure

show an ensemble of nanoparticles. A log-normal size distribution is fitted using several images to improve the statistics. The distribution results in D = 7(1) nm for OA15% 2 h and D = 8(1) nm and for OA30% 2 h (see Fig. 2). In Fig. 2b, the image shows detail of a single particle showing visible lattice planes (with a interplanar value of 0.246 nm). There is a slight deviation between the precise values of D extracted by XRD and TEM; this finding is not surprising considering that those techniques are sampling very different amounts of material (clearly XRD detects more nanoparticles) and that the TEM images (direct evidences) are compared to the result of the analysis of XRD peak broadening. Nonetheless, the important fact is that taken together both

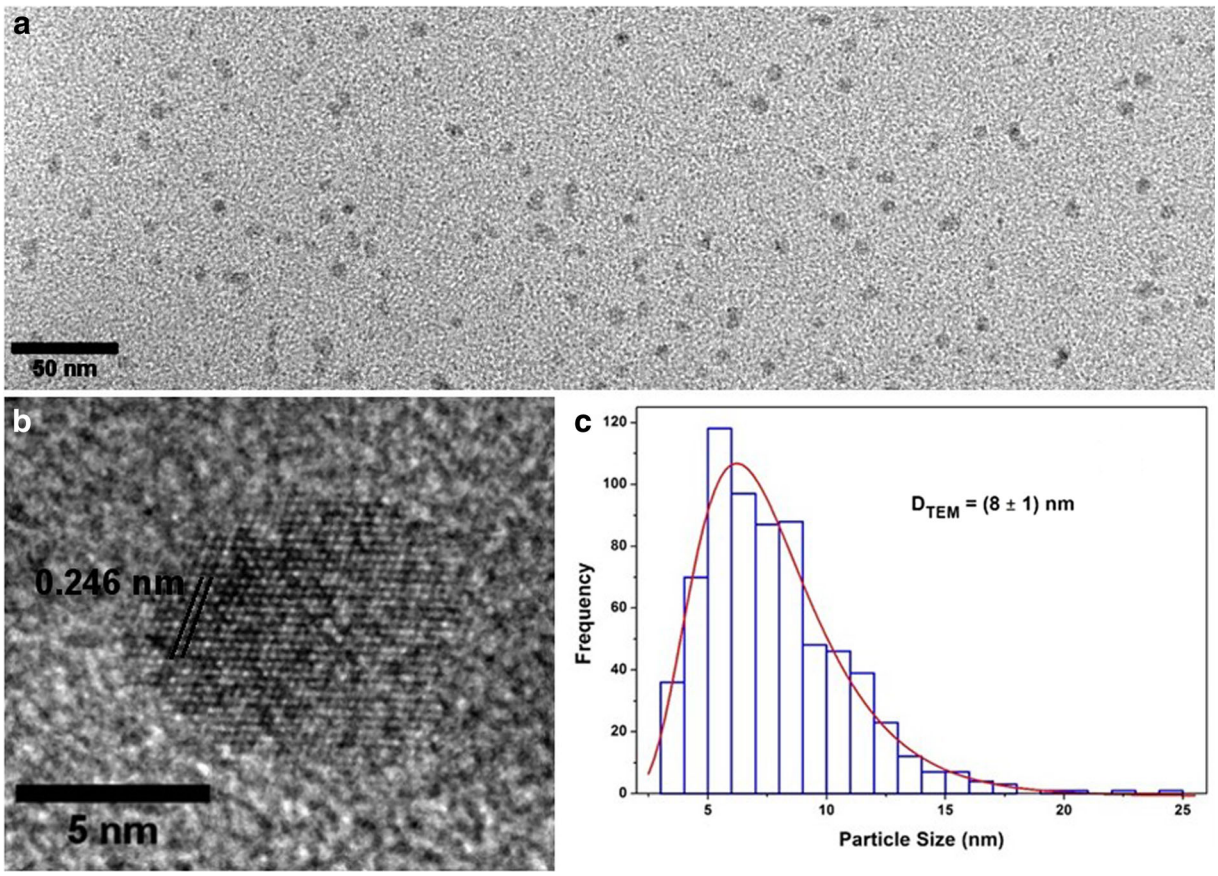

Fig. 2 **a** TEM image shows quasi-spherical surfactant-assisted $TbCu_2$ nanoparticles (OA30% 2 h sample). **b** HRTEM image of an individual particle where lattice planes are visible. **c** Particle size histograms and fit (continuous *red line*) to a log-normal distribution with $<D>$ = 8(1) nm

XRD and TEM results indicate that the use OA during milling permits the production of size-controlled ensembles of $TbCu_2$ MNPs. This confirms the complementary between both structural techniques.

For completeness, the presence of OA has been checked by Raman spectroscopy. Representative room temperature spectra are displayed in Fig. 3 for OA15% 2 h and OA15% 5 h. The phonon frequencies were obtained by fitting the experimental peaks to Lorentzian functions. Six peaks (bands) are observed with Raman shifts at 1083 cm^{-1} (C–C stretch vibration), 1265 cm^{-1} (C═C–H in plane bending), 1303 cm^{-1} ($\delta[CH_2]_n$ deformations), 1441 cm^{-1} (CH_2 scissoring), 1634 cm^{-1} (C═0 stretching) and 1653 cm^{-1} (C═C stretching). This last band is characteristic of the two mono unsaturated fatty acids. These results are in very good agreement with those published in the literature for pure OA (De Gelder et al. 2007).

The study of the magnetic properties is initiated with the variation of the DC magnetisation with field *M(H)*. In Fig. 4, *M(H)* curves are shown at T = 5 K and 40 K. On inspection of data taken at T = 5 K, every curve displays an inflection point and a continuous increase for higher values of H. The inflection points are connected with the presence of a metamagnetic transition, typical of antiferromagnets. Towards higher temperatures, the latter transition in *M(H)* is less pronounced and at T_N it disappears. These metamagnetic transitions are due to the moment flip of the sublattice in the direction of the magnetic field at H_f, and depend on the magnetocrystalline anisotropy (Luong and Franse 1995). Taking the transitions from the field-derivative *dM(H)/dH* maxima at T = 40 K (where the AFM order is well-established), we find that the values show a tendency to become lower than in bulk H_f = 19 kOe (Echevarria-Bonet et al. 2013; Luong and Franse 1995) when D is really small, with H_f = 19.5(1) kOe and H_f = 13.6(6) kOe for 2 and 5 h (OA30%). This follows the expectation that the metamagnetic transition, as studied in AFM α-Fe_2O_3 MNPs, should scale $H_f/H_{f\ bulk} \propto 1/D$. However, the decrease of H_f is very large (≈80%) on these Fe oxides compared to the present alloys (Zysler et al. 2003). If we now take the metamagnetic transition at T = 5 K (using OA30%), we deduce that H_f = 23.1(2) kOe and H_f = 24.5(2) kOe for 2 and 5 h, respectively. By contrast, there is a slight increase (29%) when the size is reduced to the nanoscale. This must be related to the additional increase of anisotropy caused by the onset of magnetic disorder of uncompensated moments promoted by the lattice strain. Following now with the continuous *M(H)* increase for $H > H_f$, it is evident that the saturation magnetization is not achieved (even for H = 14 T). Here, the maximum experimental value for the magnetisation is M = 5 μ_B/Tb, whereas theoretically $M = \mu_B\, g_J\, J = 9\ \mu_B$/Tb is expected (Landé factor: g_J = 3/2 and J = 6 for Tb). The reason for this discrepancy is the existence

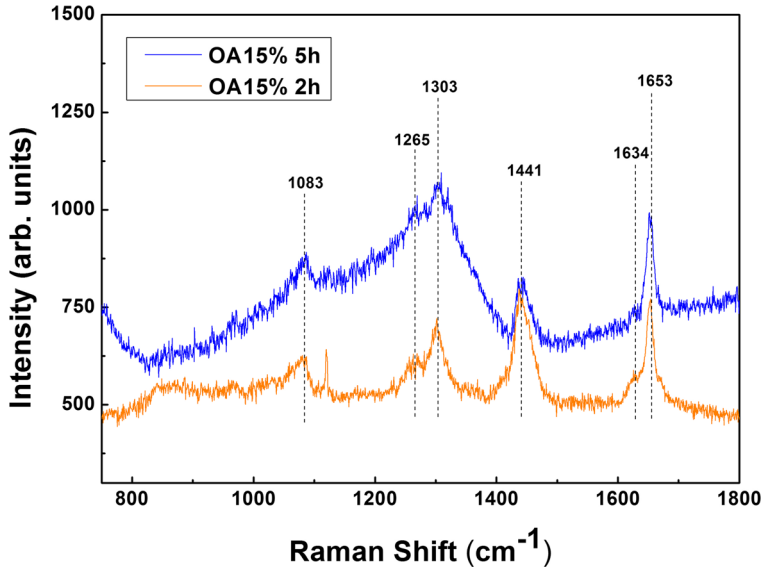

Fig. 3 Raman spectra at 300 K of representative samples. *Vertical lines* mark six bands appearing at 1083 cm^{-1} (C–C stretch vibration), 1265 cm^{-1} (C═C–H in plane bending), 1303 cm^{-1} ($\delta[CH_2]_n$ deformations), 1441 cm^{-1} (CH_2 scissoring), 1634 cm^{-1} (C═0 stretching) and 1653 cm^{-1} (C═C stretching)

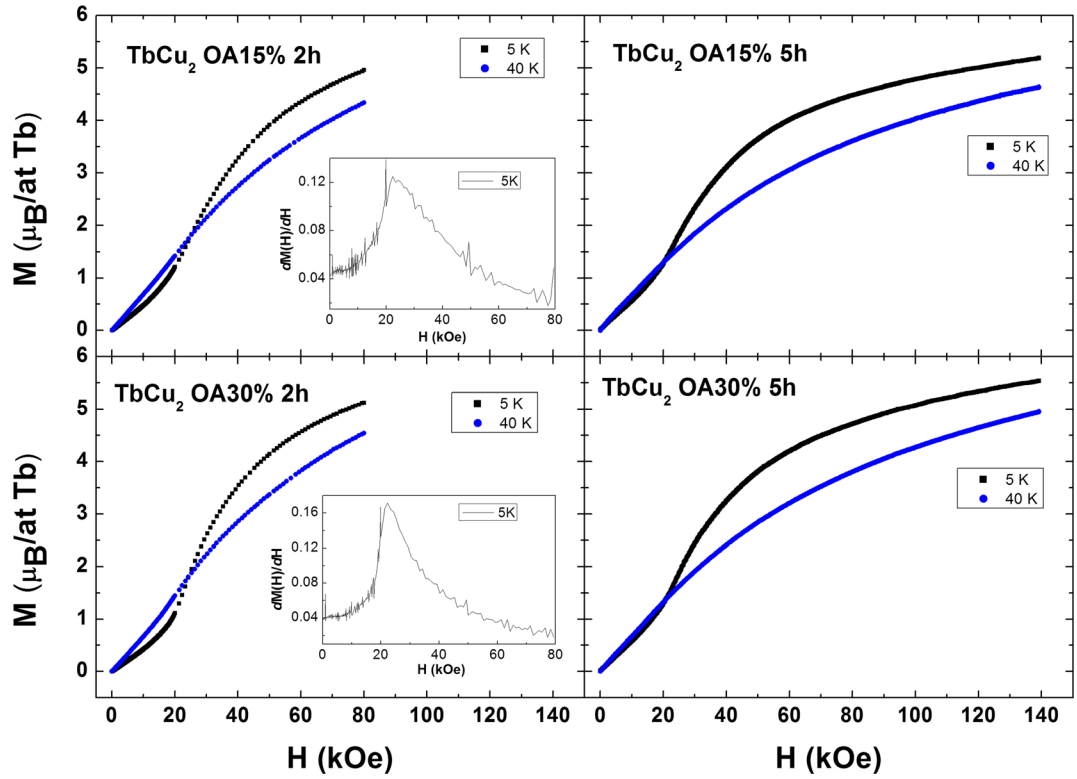

Fig. 4 Isothermal magnetisation at $T = 5$ K (*black squares*) and $T = 40$ K (*blue circles*). The metamagnetic transitions are evident for both alloys. The saturation magnetisation is not achieved due to the large magnetocrystalline anisotropy. *Insets*: examples for the derivatives *dM(H)/dH* used to obtain the magnetic field at which the metamagnetic transition takes place

of crystal electric fields, which are strong in Tb-based alloys, increasing the magnetic anisotropy. In addition, for such low temperatures, the presence of canted spins on the MNP surface exacerbates the lack of saturation.

The $M(H, T = 5\ \text{K})$ data allow a representative estimation of the number of uncompensated moments for OA15% 5 h. This can be extracted via the extrapolation of the magnetisation at zero field, resulting in $M(H = 0) = 43$ emu/g (Makhlouf Salah et al. 1997), and the density $\rho = 8.65$ g/cm^3 calculated from the lattice parameters obtained in the Rietveld refinement. Thus, the number of uncompensated moments is 15,338 μ_B/particle related to 1704 Tb^{3+} ions. The number of Tb atoms in each nanoparticle ($D = 9$ nm) is found to be about 7188. This value means that the radius of the core of the particles is around 41 Å, whereas the total nanoparticle radius is 45 Å. Essentially, with the $TbCu_2$ unit cell dimensions, the former estimation procures that a single lattice (strained) cell is the responsible for the uncompensated moments, which appears reasonable.

More information related to the presence of different magnetic phases is gathered through the study of the thermal variation of DC susceptibility $\chi_{DC}(H = 0.1$ kOe, $T)$. To obtain these data, ZFC-FC runs were recorded and are shown in Fig. 5. The samples present a major contribution with peaks at $T_N = 48.2(4)$ K (OA15% 2 h) and at $T_N = 47.7(6)$ K (OA15% 5 h), which are practically equal to OA30%. These peaks mark clearly the Néel temperatures, where the moments within the MNPs become antiferromagnetically coupled from the paramagnetic state, at which $T > T_N$. The values are practically the same as for bulk $TbCu_2$ ($T_N \approx 48.5$ K from specific heat data) (Luong and Franse 1995) and marginally higher than those of ($T_N = 46.8(5)$ K for $D = 9(1)$ nm, $t = 2$ h) the bare (surfactant-free) nano-$TbCu_2$ (Echevarria-Bonet et al. 2013). The small reduction of the Néel transition should be ascribed to finite-size effects and has been discussed in $TbAl_2$ nanoparticles as well (Rojas et al. 2012). In both insets of Fig. 5, the $1/\chi$ vs. T plot is shown, which enables the extraction of the effective Bohr magneton number of Tb (μ_{eff}) and the paramagnetic Curie temperature (θ_P). In our fits, we

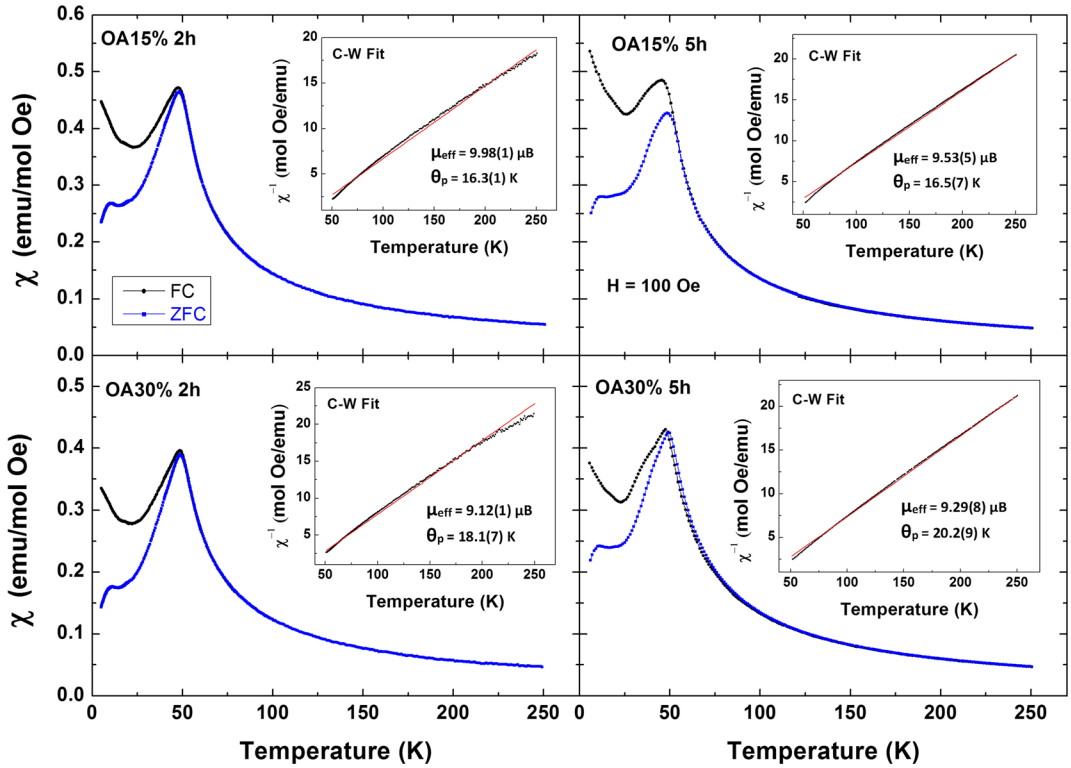

Fig. 5 DC susceptibilities χ of all samples investigated as a function of the temperature. The susceptibility presents irreversibility in the ZFC-FC branches. The increase of milling time results in a reduced peak at Néel transition and an increase of the irreversibility. Insets: χ^{-1}(T) witnessing the Curie-Weiss behaviour. The effective Bohr magneton numbers and paramagnetic Curie temperatures are displayed as well

obtain that for OA15% 2 h μ_{eff} = 9.98(1) μ_B and θ_P = 16.3(1) K and in OA15% 5 h μ_{eff} = 9.53(5) μ_B and θ_P = 16.5(7) K. These values are comparable to bare $TbCu_2$ 2 h (μ_{eff} = 9.83(5) μ_B, θ_P = 19(1) K) and $TbCu_2$ 5 h (m_{eff} = 9.99(6) μ_B, θ_P = 12.2(3) K) (Echevarria-Bonet et al. 2013). The theoretical effective Bohr magneton number of trivalent Tb (J = 6) is $\mu_{eff} = g_J\sqrt{J(J+1)}$ μ_B = 9.72 μ_B. For $T < T_N$, there is a decreasing susceptibility towards the appearance of a (broad) low-temperature peak at around 11 K (smaller magnitude than that at T_N). The origin of this peak should be related to a magnetic relaxation due to the existence of MNPs. Precisely, given that the particle presents an AFM core, the sublattice mismatch in conjunction with a shell of surface spins are responsible for this behaviour. The "broad" low-temperature peak is slightly less defined for the 2-h sample. This indicates that the relaxation is stronger when the particles are smaller. We should remind that, here, there is the advantage that bulk alloy T_N is below room temperature, in comparison to other archetypal AFM compounds in which their magnetic properties have been studied as a function of the particle size. To cite a few, NiO (T_N = 525 K) (Rinaldi-Montes et al. 2015) or α-Fe_2O_3 (T_N = 960 K) (Zysler et al. 2003).

So far, the magnetic ordering within the $TbCu_2$ nanoparticles and the relaxation process connected to the nanometric particles are both observed easily and resemble the shape of bare SAFM $TbCu_2$. However, there are hints of intriguing variations and to disclose them we ought to perform frequency-dependent thermal variation of AC susceptibility $\chi_{AC}(T,f)$ measurements. The AC susceptibility (real, χ′, and complex, χ″) components) is presented in Fig. 6 (bottom) for two ensembles of MNPs, as an example. The shape of the $\chi'(T)$ at f = 5 kHz is practically the same as the DC susceptibility with a prominent peak at T_N (≈48 K) and a low-temperature (≈15 K) broad peak at T_B (marked with an arrow). These results are consistent with the DC susceptibility findings. The dynamic (frequency) moment relaxation is shown in Fig. 6 (top) for OA15% 2 h. Clearly, the ordering temperatures do not exhibit a frequency

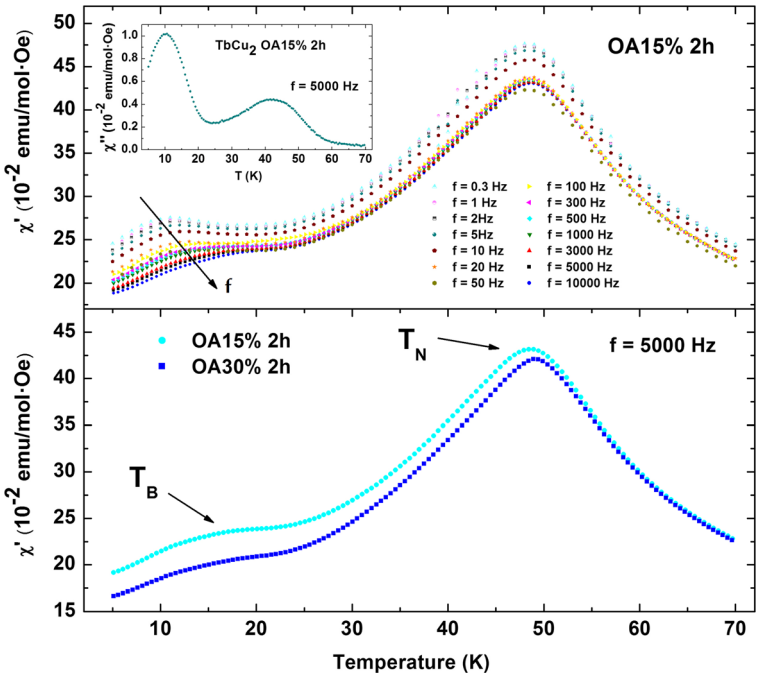

Fig. 6 *Top*: In-phase component of dynamic (AC) susceptibility of OA15% 2 h samples at 14 frequencies covering five decades. T_B marks the low-temperature relaxation process. T_N is the Néel temperature. *Top inset*: Out-of-phase component of dynamic (AC) susceptibility for OA15% 2 h. *Bottom*: Comparison of in-phase susceptibility of OA15% and OA30% 2 h with a large peak at the Néel transition (at $T \cong 48$ K) and low-T humps at $T \cong 15$ K

shift (as expected for $f < 10$ kHz), whereas the low-T peaks do visibly shift up to higher temperatures (and decrease in magnitude) with increasing f. This is a fingerprint for the existence of magnetic disorder (together to the irreversibility in ZFC-FC $M_{DC}(T)$), which in these alloys is naturally linked to the presence of MNPs. Here, the shift is quantified easily following $\delta = \Delta T_B/T_B log_{10}\omega$. In Fig. 7 (insets), there are examples of the calculation of the δ-shift which is giving $\delta = 0.09(2)$ in OA15% 2 h, $\delta = 0.11(1)$ for OA15% 5 h. Similar values are derived for OA30%, $\delta = 0.09(4)$ 2 h, $\delta = 0.11(3)$ for OA30% 5 h. In ideal superparamagnetic (SPM) systems consisting of independent single-domain MNPs, the relaxation is due to spin flipping processes. If those ones that count with thermal energy sufficient to overcome an energy barrier ($E_a = KV$) governed by the magnetic anisotropy (K) and the volume of the particles, the system is in its unblocked state (SPM regime). The relaxation process is understood with an Arrhenius equation of the form of $\tau = \tau_0 \exp.(KV/k_BT)$, with τ, the measuring time, and τ_0, the pre-exponential factor related to the attempt time (Hansen et al. 2000). In this framework $\delta = 0.1$–0.2 (Dormann et al. 1988), in the range of values encompassing those of all samples, confirming the SPM relaxation. Now, if we compare with the bare $TbCu_2$ 2 h $\delta = 0.056(3)$ (Echevarria-Bonet et al. 2015), the low-T susceptibility peak is relaxing more freely in surfactant-assisted than in those bare nanoparticles. If this is true, the analysis of the relaxation by the Arrhenius expression should give reasonable results. Accordingly, we are also introducing the revealing plot of $ln\tau$ vs. $1/T_B$ in Fig. 7. Note that number of data points is high (compared to other works) permitting a precise evaluation of parameters. The observed variations sport a linear tendency, which is validated by fits (straight line) included in the plots. The calculated values of E_a and τ_0 for 2 h samples are: OA15%: $\tau_0 = 1.3(1)\ 10^{-13}$ s and $E_a = 326(28)$ K and OA30%: $\tau_0 = 1.0(2)\ 10^{-13}$ s and $E_a = 321(66)$ K. In $t = 5$ h, OA15%: $\tau_0 = 8.4(1)\ 10^{-12}$ s and $E_a = 296(9)$ K and OA30%: $\tau_0 = 1.5(1)\ 10^{-11}$ s and $E_a = 295(16)$ K. The values for τ_0 are similar to those present in other SPM systems (Hansen et al. 2000; Kilcoyne and Cywinski 1995). The activation energies are also similar to other AFM superparamagnetic MNPs, e.g. the model system ferritin, $E_a = 318$ K, with $T_B = 15.2$–18.2 K (Kilcoyne and Cywinski 1995).

The validity of an Arrhenius relaxation is consistent with the δ-shift values and contrasts with the same analysis for bare $TbCu_2$. Indeed, in the latter analyses, it was clear that the relaxation was connected to a spin glass environment and that the moment relaxation process could be understood under the critical slowing down model assumptions (Echevarria-Bonet et al.

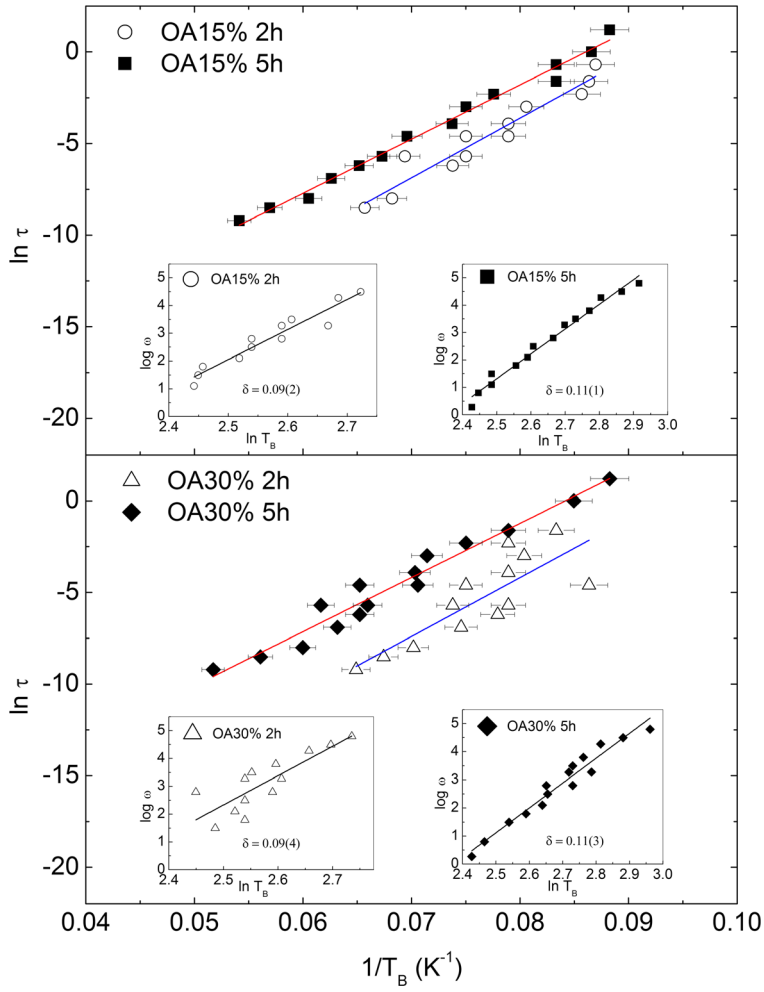

Fig. 7 Arrhenius plots (ln τ vs. $1/T_B$) for OA15% and OA30% 2 h and 5 h nano-$TbCu_2$ samples. These exhibit a linear behaviour (with no less than 12 *f*-values) typical of superparamagnetic relaxation. Calculated activation energies (E_a) and relaxation rate (τ_0) values are given in the text. Insets show the extraction of the δ-shift parameter

2015). In these, the Tb moment–moment correlation length becomes divergent in the vicinity of the freezing temperature. This model is also obeyed by other very different NiO (2–10 nm) particles pointing to a rather universal behaviour in AFM nanoparticles. In those Ni oxide MNPs, a magnetically disordered distribution of Ni^{3+} atoms is decorating the particle surface (Rinaldi-Montes et al. 2015). This is not the case here, and as a matter of fact, it is necessary to invoke the presence of the surfactant layers of oleic acid. The latter is obviously a diamagnetic material interrupting the magnetic coupling of neighbouring mismatched moments. The existence of a truly Arrhenius behaviour should be due to the absence (or negligible) of magnetic interparticle interactions, and hence, the existing SAFM state should also be weakened by the surfactant. In fact, dipolar interactions are known to be reduced in AFM MNPs with respect to those in nanoparticles with a ferro- or ferri-magnetic core (Mørup et al. 2011; Hansen et al. 2000). As a consequence, we observe a cutoff of the interactions, which were indeed present for the bare $TbCu_2$ nanoparticles.

Conclusions

Nanoparticles of $TbCu_2$ with oleic acid have been produced by the surfactant-assisted milling route. This route enables control of nanoparticles size requiring longer times than bare nano-$TbCu_2$ to reach similar values. All the basic crystallographic parameters (group symmetry, atomic positions) remain equal to those of bulk $TbCu_2$, giving only slightly lower values for lattice volume. The MNPs present a core with an antiferromagnetic structure and a disordered environment promoted by a lattice mismatch and a shell disorder. The

metamagnetic transition (slight decrease) and the Néel temperature (finite-size reduction) are both affected by the reduction of size with a slight variation. This is pointing to a small reduction of Tb^{3+}–Tb^{3+} indirect (RKKY) exchange and to an increase of anisotropy, respectively.

The effect of the surfactant is reflected particularly in the moment dynamics of the low-temperature blocking peaks. Thus, the magnetic relaxation of MNPs becomes independent and governed by an energy barrier and Arrhenius model, contrary to the spin glass-like behaviour found in bare superantiferromagnetic $TbCu_2$ nanoparticles counterparts. It is then worth mentioning that this production route enables to modify drastically the magnetic coupling and may constitute a path to isolate completely *R*-based nanoparticles.

Acknowledgments This work has been supported by Spanish MINECO grant MAT2014-55049-C2-R. M. de la Fuente Rodríguez work is also supported by FPI (BES-2012-058722).

Compliance with ethical standards The authors declare that they have no conflict of interest.

References

Akdogan NG, Hadjipanayis GC, Sellmyer DJ (2009) J Appl Phys 105:07A710

Alba Venero D, Fernández Barquín L, Alonso J, Fdez-Gubieda ML, Rodríguez Fernández L, Boada R, Chaboy J (2013) J Phys Condens Matter 25:276001

Andersson MS, Mathieu R, Su Seong L, Normile PS, Singh G, Nordblad P, De Toro JA (2015) Nanotechnology 26:475703

Bedanta S, Kleemann W (2009) J Phys D Appl Phys 42:013001

Berry CC, Curtis ASG (2003) J Phys D Appl Phys 36:R198

Chandra S, Khurshid H, Li W, Hadjipanayis GC, Phan MH, Srikanth H (2012) Phys Rev B 86:014426

Coey J M D (2010) Magnetism and magnetic materials (Cambridge University press)

Cuellar FA, Liu YH, Salafranca J, Nemes N, Iborra E, Sanchez-Santolino G, Varela M, Garcia Hernandez M, Freeland JW, Zhernenkov M, Fitzsimmons MR, Okamoto S, Pennycook SJ, Bibes M, Barthélémy A, te Velthuis SGE, Sefrioui Z, Leon C, Santamaria J (2014) Nat Commun 5:52153

De Gelder J, De Gussem K, Vandenabeele P, Moens L (2007) J Raman Spectrosc 38:1133

De Paula VG, da Silva LM, dos Santos AO, Lang R, Otubo L, Coelho AA, Cardoso LP (2016) Phys Rev B 93:094427

Dormann JL, Bessais L, Fiorani D (1988) J Phys C Solid State Phys 21:2015

Echevarria-Bonet C, Rojas DP, Espeso JI, Rodríguez Fernández J, Rodríguez Fernández J, Gorria P, Blanco JA, Fdez-Gubieda ML, Bauer E, André G, Fernández Barquín L (2013) Phys Rev B 87:180407(R)

Echevarria-Bonet C, Rojas DP, Espeso JI, Rodríguez Fernández J, de la Fuente RM, Fernández Barquín L, Rodríguez Fernández L, Gorria P, Blanco JA, Fdez-Gubieda ML, Bauer E, Damay F (2015) J Phys Condens Matter 27:496002

Estrader M, López-Ortega A, Estradé S, Golosovsky IV, Salazar-Alvarez G, Vasilakaki M, Trohidou KN, Varela M, Stanley DC, Pechan MJ, Keavney DJ, Peiró F, Surinach S, Baró MD, Nogués J (2013) Nat Commun 4:2960

Gleiter H, Schimmel T, Hahn H (2014) Nano Today 9:17–68

Hansen MF, Koch CB, Mørup S (2000) Phys Rev B 62:1124

Kilcoyne SH, Cywinski R (1995) J Magn Magn Mater 1466:140–144

Li WF, Hu XC, Cui BZ, Yang JB, Han JZ, Hadjipanayis GC (2013) J Magn Magn Mater 339:71

Lu AH, Salabas EL, Schuth F (2007) Angew Chem Int Edn Engl 46:1222

Luong N H and Franse J (1995) Handbook of magnetic materials: magnetic properties of rare Earth-Cu2 compounds. In: Buschow K H J (ed) vol 8. Elsevier, Amsterdam, p 415

Makhlouf Salah A, Parker FT, Berkowitz AE (1997) Phys Rev B 55:R14717

Morales MA, Williams DS, Shand PM, Stark C, Pekarek TM, Yue LP, Petkov V, Leslie-Pelecky DL (2004) Phys Rev B 70: 184407

Moriarty P (2001) Rep Prog Phys 64:297

Mørup S, Madsen MB, Franck J, Villadsen J, Koch CJW (1983) J Magn Magn Mater 40:163

Mørup S, Hansen MF, Frandsen C (2011) Comprehensive nanoscience and Nanotechnology, vol 1. Academic, Oxford, p 437

Nogués J, Sort J, Langlais V, Skumryev V, Suriñach S, Muñoz JS, Baró MD (2005) Phys Rep 422:65

Peddis D, Rinaldi D, Ennas G, Scano A, Agostinelli E, Fiorani D (2012) Phys Chem Chem Phys 14:3162

Rinaldi-Montes N, Gorria P, Martínez-Blanco D, Fuertes AB, Fernández Barquín L, Puente-Orench I, Blanco JA (2015) Nanotechnology 26:305705

Rodríguez-Carvajal J (1993) Physica B 192:55

Rojas DP, Fernández Barquín L, Rodríguez Fernández J, Espeso JI, Gómez Sal JC (2007) J Phys Condens Matter 19:186214

Rojas DP, Fernández Barquín L, Echevarria-Bonet C, Rodríguez Fernández J (2012) J Nanosci Nanotechnol 12:7482

Sánchez-Valdés CF, Ibarra-Gaytán PJ, Sánchez Llamazares JL, Ávalos-Borja M, Álvarez-Alonso P, Gorria P, Blanco JA (2014) Appl Phys Lett 104:212401

Schneider CA, Rasband WS, Eliceiri KW (2012) Nat Methods 9: 671

Simeonidis K, Sarafidis C, Papastergiadis E, Angelakeris M, Tsiaoussis I, Kalogirou O (2011) Intermetallics 19:589

Stark WJ, Stoessel PR, Wohlleben W, Hafner A (2015) Chem Soc Rev 44:5793–5805

Tartaj P, Morales MD, Veintemillas-Verdaguer S, Gonzalez-Carreno T, Serna CJ (2003) J Phys D Appl Phys 36(13):R182

Ullah M, Eaqub AM, Hamid SBA (2014) Rev Adv Mater Sci 37:1

Wang Y, Li Y, Rong C, Liu JP (2007) Nanotechnology 18:465701

Yadav TP, Yadav RM, Singh DP (2012) Nanosci Nanotechnol 2: 22

Zhou GF, Bakker H (1995) Phys Rev B 52:9437

Zysler RD, Fiorani D, Testa AM, Suber L, Agostinelli E, Godinho M (2003) Phys Rev B 68 (21):212408